



Mechanism and Control Methods of Roof Deformations in Gob-Side Entry Retention by Roof Cutting Under Medium-Thick Coal Seams

Xiaojie Yang · Wenbin Mao · Eryu Wang · Yue Sun · Jiamin Wang · Manchao He

Received: 11 March 2019 / Accepted: 1 August 2019 / Published online: 6 August 2019
© Springer Nature Switzerland AG 2019

Abstract In order to ensure the successful implementation of gob-side entry retention by roof cutting under medium-thickness coal seams and compound roof conditions in Guandi Coal Mine, a mechanical model was established to analyze the factors affecting the roof deformation, and the roof fracturing height and roof fracturing direction were researched by way of numerical simulation and field experiments. The theoretical analysis and numerical simulation showed that the rotation angle of the upper main roof is the main factor leading to roof deformation, that increasing the support strength in the roadway cannot reduce the roof deformation, and that the roof deformation can be effectively controlled by increasing the roof fracturing height and the fracturing direction. The results confirmed that the roof fracturing height was 7 m, the roof fracturing direction was 15°, and the

charging structure was 3 + 3 + 2 + 1. The roof was strengthened using a constant resistance and large deformation anchor, a single hydraulic prop reinforcement support in the lane, and a U-shaped steel retaining gangue support. The retained entry was stable at 200 m behind the working face and can meet the demands of reuse for the next mining face.

Keywords Coal resources · Roof cutting and pressure release · Mechanical model · Numerical simulation · Surrounding rock control

1 Introduction

After decades of large-scale mining, China's shallow coal resources are facing a crisis of exhaustion. In the past, the traditional longwall mining mode has caused the wastage of coal resources and frequent disasters, and it has seriously hindered the development of the coal industry. In order to rid the coal industry of the trouble caused by traditional mining methods, scholars at home and abroad have performed much research on non-pillar mining techniques and achieved fruitful results; in particular, the theoretical analysis and technical applications of Gob-side Entry Retaining (GER) have developed rapidly. For example, Zhang et al. (2012) analyzed the stability of a retained gob-side entry and evaluated the influencing factors of roadway deformation. Zhang et al. (2018) deduced the shear strength of

X. Yang · W. Mao (✉) · Y. Sun · J. Wang · M. He
State Key Laboratory for Geomechanics and Deep
Underground Engineering, China University of Mining
and Technology, Beijing 100083, China
e-mail: 1872346351@qq.com

X. Yang · W. Mao · Y. Sun · J. Wang · M. He
School of Mechanics and Civil Engineering, China
University of Mining and Technology, Beijing 100083,
China

E. Wang
Institute of Mining Research, Inner Mongolia University
of Science and Technology,
Baotou 014010, Inner Mongolia, China

the shear sliding zone above a roadside backfill area considering rockbolt support. Deng and Wang (2014) analyzed the stress and deformation process of roof strata by theoretical analysis and numerical simulation. Lin and Shi (2012) researched walling-up with concrete blocks in gob-side entry retaining based on a fully mechanized face in a medium-thickness coal seam. Yang et al. (2016) evaluated the adaptation of gob-side entry retaining by using a 1–9 scale method of the analytic hierarchy process. Xu et al. (2016) innovatively proposed a new approach, named the steel pile method, to control severe floor heaves in gob-side entry retaining. Zhang et al. (2015) designed a rational roadside backfill body (RBB) with high-water quick-setting materials using a numerical model. Wang et al. (2014) designed a dual-function supporting and filling formwork support and studied the motion trajectory of the roof. Waclawik et al. (2017) revealed the stress state of a rock mass caused by longwall mining and its variation law by monitoring the stress change of the rock mass in a working face. Han et al. (2018a, b) researched the characteristics of gob-area sequential roof collapse of overlying strata and the superposed disturbance mechanism for gob-side entry retaining via physical simulation and theoretical analysis. Han et al. (2018a, b) determined two characteristics of stratum movement after mining that have a great influence on GER in a physical simulation experiment. The above studies have promoted the development of the coal mining industry, improved the coal recovery rate, and eliminated the coal pillar. However, the low strength and high cost of the filling materials and the stress concentration in the filling body severely restrict their development.

In order to solve the problems caused by the traditional gob-side entry retaining technology, the “Cutting Cantilever Beam Theory” (CCBT) and Gob-side Entry Retaining by Roof Cutting (GERRC) non-pillar mining technology were first proposed in 2008 (He et al. 2015). Gob-side entry retention by roof cutting changes the structure of the roadway roof and goaf roof by directional energy-accumulating blasting, and it realizes goaf-side roadway protection and pillar-free mining by utilizing the collapse and swelling of the goaf roof. Therefore, it has the advantages of increasing the coal recovery rate, reducing the risk of roadway disasters, prolonging the service life of the mine, reducing the amount of roadway excavation, and achieving Y-type ventilation. After more than 10 years of theoretical research and field tests, the technology has

been successfully tested in China. Wang et al. (2018) explored the relationship between the roof deformation and main influence parameters by theoretical analysis. Ma et al. (2018a, b) studied the effect of coal seam inclination on the roof slit depth and angle. Sun et al. (2014) studied the key parameters in gob-side entry retaining formed by roof cutting and pressure release in thin coal seams. In recent years, researchers have performed much research on the key technology of GERRC (Gao et al. 2018; Guo et al. 2016; Chen et al. 2016; Ma et al. 2018a, b), perfecting the new mining method, and this technology has been successfully applied in many mines. However, little research has been done on the factors affecting roof deformation under the new technology (Gao et al. 2017; Wang et al. 2018; Ma et al. 2017). Based on the conditions of a composite roof and a medium-thickness coal seam in Guandi Coal Mine, this paper mainly studies the factors affecting roof deformation and the key parameters of gob-side entry retention by roof cutting. The research results provide a reference for this new non-pillar mining technique under similar geological conditions.

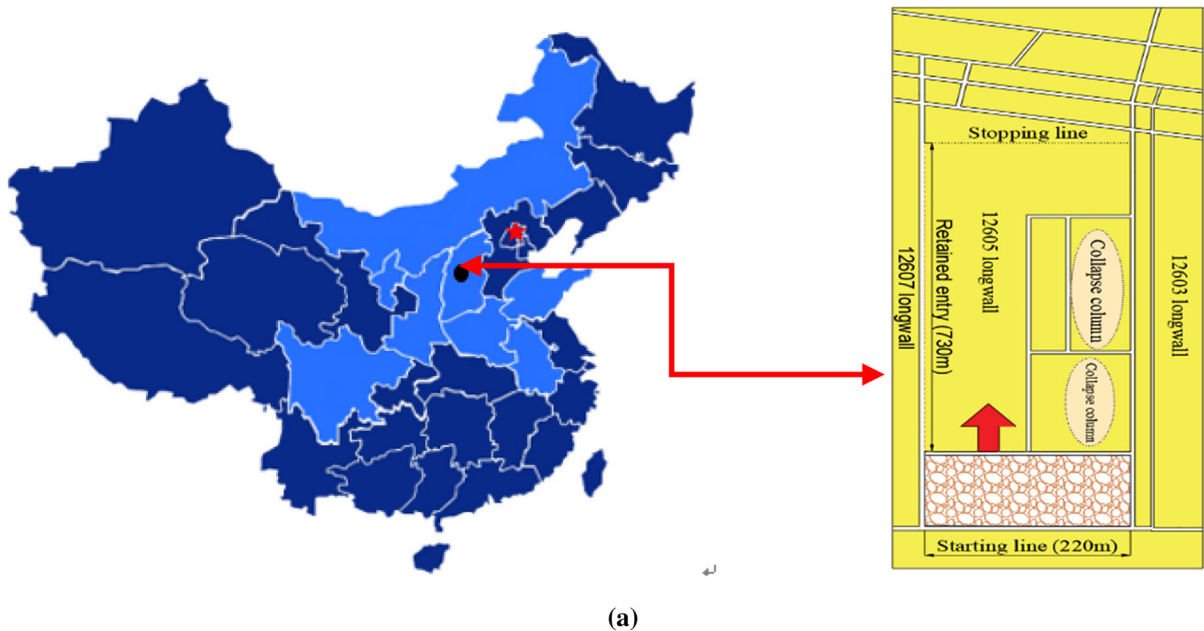
2 General Situation of the Project

Guandi Coal Mine is located in Taiyuan City, Shanxi Province, China. The 12,605 working face is located at the southeast side of the belt lane, the northeast side of the working face is the 12,603 working face, and the southwest side is an unmined area. The longwall working face is approximately 931 m in length and 220 m in width, and its layout is shown in Fig. 1a. The coal seam is 2.4 m thick and the average buried depth is 316 m. The average coal seam inclination is 5°. The immediate roof and floor are carbonaceous mudstone and mudstone, the main roof is Sand mudstone interbed and medium sandstone, and the main floor is medium sandstone; the roof lithologic profile is shown in Fig. 1b, and the relevant parameters of each rock layer are listed in Table 1.

3 Principle and Process of GERRC

3.1 The Principle of GERRC

Based on the “Cutting Cantilever Beam Theory” (CCBT), the stress transfer between the roof of the gob



Columnar	Thickness (m)	Lithology
	9.29	Siltstone
	3.24	Mudstone
	2.05	Medium sandstone
	6.34	Sand mudstone interbed
	0.60	Carbonaceous mudstone
	2.81	Coal
	0.60	Mudstone
	10.37	Medium sandstone

Fig. 1 Layout and roof lithology of the 12,605 longwall working face. **a** Layout of the 12,605 longwall working face. **b** Lithological profile

and the roof of the roadway is cut off by directional cumulative tensile blasting technology. At the same time, the roof of the roadway is strengthened by a constant resistance and large deformation anchor (CRLDA). After the working face is pushed over, the roof of the gob collapses along the blasting crack and provides a good support for the main roof. Finally, the surrounding rock of the roadway is stable under the

collective effect of the constant resistance and large deformation anchor, the gangue, and the inner support (He et al. 2017a, b).

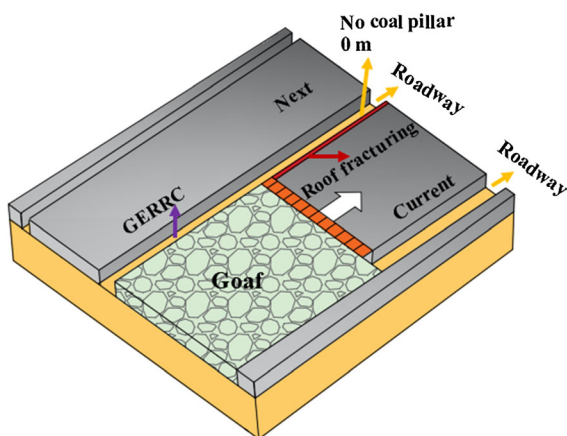
3.2 The Process of GERRC

To ensure the success of this technology under the conditions of a medium-thickness coal seam and a

Table 1 Parameters of the roof layers

Lithology	Density (kg m ⁻³)	Bulk modulus (GPa)	Shear modulus (GPa)	Tensile strength (MPa)	Cohesion (MPa)	Internal friction angle (°)
Siltstone	2760	7.10	6.82	1.33	3.46	34
Mudstone	2450	6.25	3.09	6.40	1.54	28
Medium sandstone	2730	6.99	5.46	1.05	2.63	30
Stand mudstone interbed	2610	7.00	4.59	8.80	2.55	26
Carbonaceous mudstone	2560	5.59	2.96	6.10	1.66	27
Coal	1450	5.70	2.48	5.20	1.06	25
Mudstone	2450	6.25	3.09	6.40	1.54	28
Medium sandstone	2730	6.99	5.46	1.05	2.63	30

composite roof, GERRC is divided into the following five steps: firstly, a constant resistance and large deformation anchor is installed on the roof of the roadway to strengthen the roof of the roadway. Secondly, the roof of the roadway is drilled along the side of the gob, and the hole is filled with a concentrating blasting device for directional cumulative tensile blasting. Thirdly, the support of the roof is reinforced with a single prop within a certain distance of the advanced working face. Fourthly, after the work surface is pushed over, the gangue support is added in time. Fifthly, the roof of the gob is collapsed to fill the gob under self-weight and the main roof pressure, and the entry is finally retained (He et al. 2017a, b). A schematic diagram of non-pillar mining with GERRC is shown in Fig. 2 (He et al. 2018a, b).

**Fig. 2** A schematic diagram of non-pillar mining with gob-side entry retention by roof cutting (GERRC)

4 Establishment and Solution of the Roof Mechanics Model

4.1 Mechanical Model

In order to study the deformation law of the roadway roof under this new technology, a mechanical model was established to analyze the factors affecting the deformation of the roadway roof. A large amount of elastic deformation energy will accumulate in the immediate roof under the combined action of overlying strata compression and supporting resistance. Therefore, the immediate roof is regarded as a deformable body, and the displacement variational method is used to solve the roof subsidence problem of the roadway (He et al. 2018a, b). Based on the proposed overall mechanical model of support-surrounding rock (Qian et al. 1996; Qian and Miao 1996), a mechanical model of the roof was established. At this time, the roof of the roadway can be regarded as a cantilever beam, the left boundary of the roof as a fixed boundary, the right boundary as a stress boundary under the effect of the gangue support (i.e., p_2), and the upper boundary as a given deformation boundary for the main roof. The displacement boundary condition is given, and the lower boundary is the stress boundary under the effect of a temporary support system (i.e., p_1) (Gao et al. 2000; Lu et al. 2011). The mechanical model of a short cantilever beam is shown in Fig. 3.

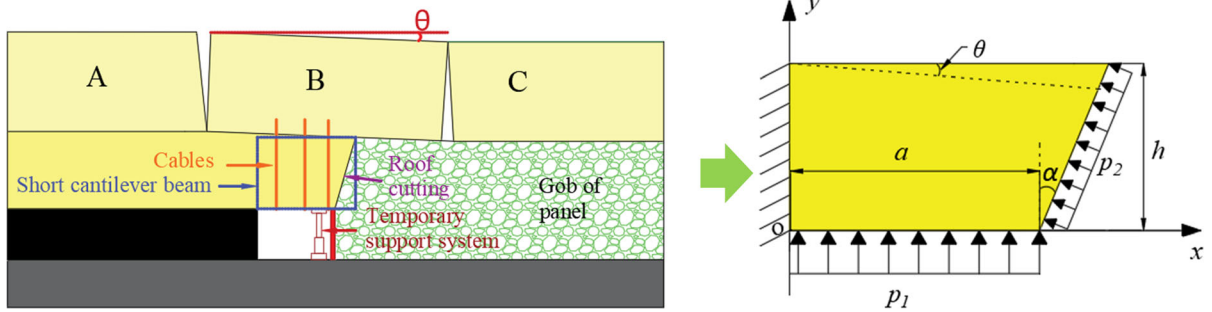


Fig. 3 Mechanical model of a short cantilever beam

4.2 Displacement Variational Method

Under a general stress state, the deformation potential energy stored in an elastomer is

$$U = \frac{1}{2} \iiint \sigma \epsilon dv. \tag{1}$$

Assuming that the roof is infinitely long in the z direction and is a plane strain problem, the displacement component can be expressed as.

$$U = \frac{E}{2(1+\mu)} \iint \left[\frac{\mu}{(1-\mu)} \left(\frac{\partial u}{\partial x} + \frac{\partial v}{\partial y} \right)^2 + \left(\frac{\partial u}{\partial x} \right)^2 + \left(\frac{\partial v}{\partial y} \right)^2 + \frac{1}{2} \left(\frac{\partial u}{\partial y} + \frac{\partial v}{\partial x} \right)^2 \right] dx dy. \tag{2}$$

The expression of the displacement component is as follows:

$$\begin{aligned} u &= u_0 + \sum_m A_m u_m, \\ v &= v_0 + \sum_m B_m v_m, \end{aligned} \tag{3}$$

where u_0 and v_0 are set functions satisfying the boundary conditions, u_m and v_m are functions equal to 0 on the boundary, and A_m and B_m are undetermined constants.

The displacement variational equations for solving A_m and B_m are then obtained:

$$\begin{aligned} \frac{\partial U}{\partial A_m} &= \iint X u_m dx dy + \int \bar{X} u_m ds, \\ \frac{\partial U}{\partial B_m} &= \iint Y v_m dx dy + \int \bar{Y} v_m ds. \end{aligned} \tag{4}$$

4.3 Problem Solution

According to the mechanical model of the roof, the body force component is

$$\begin{cases} f_x = 0 \\ f_y = -\rho g \end{cases} \tag{5}$$

the area force boundary conditions are

$$\begin{cases} \bar{f}_x = -p_2 \cos \alpha, x = a + y \tan \alpha \\ \bar{f}_y = p_2 \sin \alpha, x = a + y \tan \alpha \\ \bar{f}_x = 0, y = 0 \\ \bar{f}_y = p_1, y = 0 \end{cases} \tag{6}$$

and the displacement boundary conditions are

$$\begin{cases} u = v = 0, x = 0 \\ v = -x\theta, y = h \end{cases} \tag{7}$$

where θ is the rotation angle of the upper main roof; a is the entry width; h is the roof fracturing height; α is the roof fracturing angle; u is the horizontal displacement; and v is the vertical displacement of the short cantilever beam.

In order to satisfy the above conditions given by Eqs. (5)–(7), the displacement component is expressed as

$$\begin{cases} u = Ax \\ v = -x\theta + B \frac{x}{a} \left(1 - \frac{y}{h} \right) \end{cases} \tag{8}$$

where A and B are the undetermined constants.

Obviously, the above formulas satisfy the displacement boundary conditions of the problem and can be solved by the Rayleigh–Ritz method. For plane strain problems, the elastic potential energy of a cantilever beam is

$$\begin{aligned}
 U &= \frac{E}{2(1+\mu)} \int_0^h \int_0^{a+y \tan \alpha} \left[\frac{\mu}{(1-\mu)} \left(\frac{\partial u}{\partial x} + \frac{\partial v}{\partial y} \right)^2 + \left(\frac{\partial u}{\partial x} \right)^2 + \left(\frac{\partial v}{\partial y} \right)^2 + \frac{1}{2} \left(\frac{\partial u}{\partial y} + \frac{\partial v}{\partial x} \right)^2 \right] dx dy \\
 &= \frac{E}{2(1+\mu)} \left[\frac{A^2(2ah + h^2 \tan \alpha)}{2(1-\mu)} \right. \\
 &\quad - \frac{\mu}{1-\mu} \frac{AB(3a^2 + 3ah \tan \alpha + h^2 \tan^2 \alpha)}{3a} \\
 &\quad + \frac{1}{(1-\mu)} \frac{B^2(4a^3 h^{-1} + 6a^2 \tan \alpha + ah \tan^2 \alpha + h^2 \tan^3 \alpha)}{12a^2} \\
 &\quad + \frac{B^2(4ah + h^2 \tan \alpha)}{24a^2} - \frac{B\theta(3ah + h^2 \tan \alpha)}{6a} \\
 &\quad \left. + \frac{\theta^2(2ah + h^2 \tan \alpha)}{4} \right]. \tag{9}
 \end{aligned}$$

Using the Rayleigh–Ritz displacement variational method, simultaneous equations of the undetermined constants A and B are established as follows:

$$\begin{aligned}
 \frac{E}{2(1+\mu)} \left[\frac{A(2ah + h^2 \tan \alpha)}{1-\mu} \right. \\
 \left. - \frac{\mu}{1-\mu} \frac{B(3a^3 + 3ah \tan \alpha + h^2 \tan^2 \alpha)}{3a} \right] \\
 = - \frac{(2ah + h^2 \tan \alpha)p_2 \cos \alpha}{2} \tag{10}
 \end{aligned}$$

$$\begin{aligned}
 \frac{E}{2(1+\mu)} \left[- \frac{\mu}{1-\mu} \frac{A(3a^2 + 3ah \tan \alpha + h^2 \tan^2 \alpha)}{3a} \right. \\
 + \frac{1}{(1-\mu)} \frac{B(4a^3 h^{-1} + 6a^2 \tan \alpha + ah \tan^2 \alpha + h^2 \tan^3 \alpha)}{6a^2} \\
 + \frac{B(4ah + h^2 \tan \alpha)}{12a^2} - \frac{\theta(3ah + h^2 \tan \alpha)}{6a} \left. \right] = \\
 - \frac{\rho g(6a^2 h + 4ah^2 \tan \alpha + h^3 \tan^2 \alpha)}{24a} \\
 + \frac{1}{2} a(p_1 a + p_1 l) \left(1 - \frac{y}{h} \right) \\
 + \left[\frac{(a + h \tan \alpha)^2}{2a} - \frac{(a + h \tan \alpha)^3}{3ah \tan \alpha} \right] p_2 \sin \alpha. \tag{11}
 \end{aligned}$$

This is the binary first-order equation system of A and B. After solving for A and B, the expression of the immediate roof displacement component can be obtained. Because the expressions A and B are extremely lengthy, they are not given here.

5 Influencing Factors of Roof Subsidence in GERRC

According to the actual situation of the 12,605 working face of Guandi Coal Mine, we set $a = 4$ m, $\rho g = 21 \times 10^3$ kN/m³, $h = 5$ – 10 m, $\theta = 1^\circ$ – 7° , $E = 6$ GPa, $\mu = 0.3$, $p_1 = 1.2$ MPa, $p_2 = 0.03$ MPa, and $\alpha = 5^\circ$ – 20° . The roof of the roadway has the largest amount of subsidence on the side of the gob; therefore, the relationships between the subsidence of the roof on the side of the gob and the support resistance, the rotation angle of the upper main roof, the roof fracturing height, and the roof fracturing direction are discussed.

5.1 Relationship Between Roof Subsidence and Support Resistance

Take $h = 5$ m, $\alpha = 10^\circ$, and $\theta = 5^\circ$; then, the expression relating support resistance and roof subsidence is shown in Eq. (10), and the curve of roof subsidence against support resistance shown in Fig. 4 was obtained by using Eq. (10).

$$v = 0.1988 - 0.0013p_1 \tag{12}$$

In Fig. 4, the relationship between roof subsidence and roadway support strength is approximately linear; as the support strength increases, the roof subsidence decreases slightly. For instance, when the support strength is 0.2 MPa, the roof subsidence is 199 mm; however, when support strength is 1.2 MPa, the roof

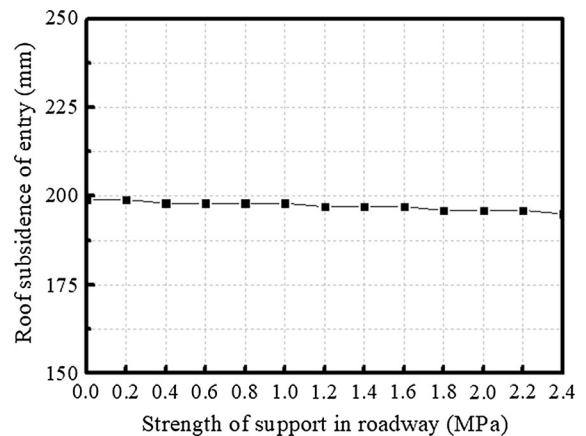


Fig. 4 Relationship between roof subsidence and support resistance

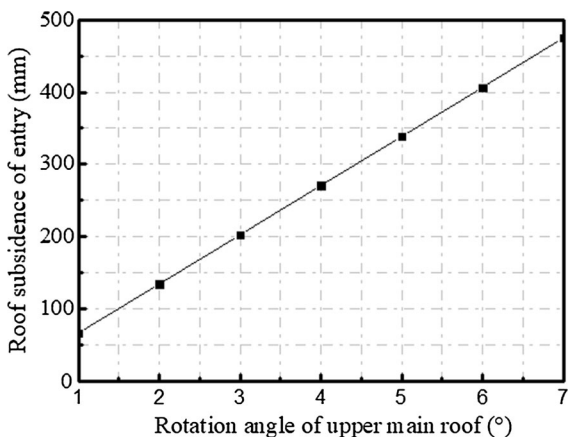


Fig. 5 Relationship between roof subsidence and the rotation angle of the upper main roof

subsidence is 197 mm. Therefore, the support resistance cannot effectively control roof subsidence.

5.2 Relationship Between Roof Subsidence and the Rotation Angle of the Upper Main Roof

Take $h = 5$ m and $\alpha = 10^\circ$; then, the expression relating the rotation angle of the upper main roof and roof subsidence is shown in Eq. (11), and the curve of roof subsidence against the rotation angle of the upper main roof was obtained by using Eq. (11), as shown in Fig. 5.

$$v = 0.001331 - 4\theta \tag{13}$$

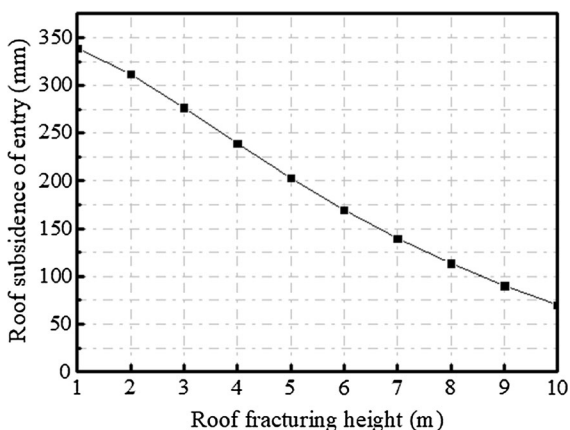


Fig. 6 Relationship between roof subsidence and roof fracturing height

As can be seen in Fig. 5, the roof subsidence increases linearly with increasing rotation angle. For example, the subsidence value of the roof is only 66.67 mm with a 1° rotation angle; however, it increases obviously to 474.67 mm with a 7° rotation angle. This shows that the rotation angle has a significant effect on roof subsidence.

5.3 Relationship Between Roof Subsidence and the Roof Fracturing Height

Take $\alpha = 10^\circ$ and $\theta = 5^\circ$; then, the expression relating the roof fracturing height and roof subsidence is shown in Eq. (12), and the curve of roof subsidence against roof fracturing height is shown in Fig. 6.

$$v = -0.35 + \frac{0.001h^4 + 0.079h^3 + 1.41h^2 + 0.067h}{0.002h^4 + 0.158h^3 + 3.62h^2 + 16.45h + 119.84} \tag{14}$$

Figure 6 shows that the relationship between roof subsidence and the roof fracturing height is approximately linear, and the roof subsidence decreases with increasing roof fracturing height. For instance, when the roof fracturing height is 1 m, the value of roof subsidence is 338.88 mm, while the roof subsidence is only 70.18 mm with a roof fracturing height of 10 m. It is obvious that increasing the roof fracturing height can effectively control the deformation of the roof.

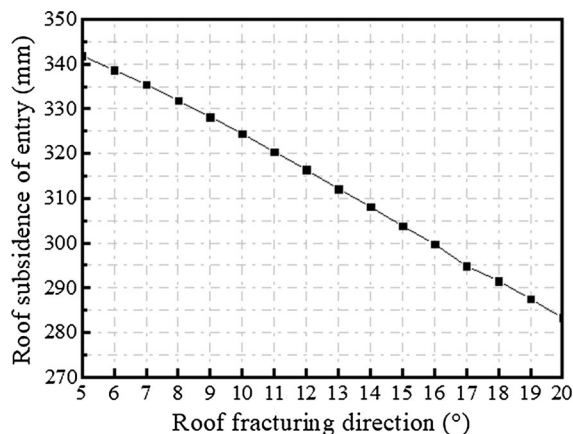


Fig. 7 Relationship between roof subsidence and the roof fracturing direction

5.4 Relationship Between Roof Subsidence and the Roof Fracturing Direction

Take $h = 5$ m, and $\theta = 5^\circ$; then, the expression relating the roof fracturing direction and roof subsidence is shown in Eq. (13), and the curve of roof subsidence against the roof fracturing direction is shown in Fig. 7.

$$v = -0.35 + \frac{9 \times 10^{-5} \cos \alpha + 5 \times 10^{-4} \sin \alpha + 4.765 \tan \alpha \sin \alpha + 6 \times 10^{-5} \cos \alpha + 2.978 \sin \alpha \tan^2 \alpha}{1.759 \tan^4 \alpha + 8.464 \tan^3 \alpha + 16.379 \tan^2 \alpha + 13.746 \tan \alpha + 3.342} \quad (15)$$

As can be seen in Fig. 7, the roof subsidence decreases linearly with increasing roof fracturing direction. For example, the roof subsidence is close to 342 mm with a 5° roof fracturing angle, while the roof subsidence is only 283 mm when the cutting angle is 2° . However, as can be seen from Fig. 7, the reduction in roof subsidence is not obvious with an increased cutting angle. This shows that the roof fracturing direction has little influence on the deformation of the roof.

6 FLAC3D Numerical Simulation Analysis

According to the engineering geological conditions of the 12,605 working face of Guandi Coal Mine combined with the results of ground stress monitoring,

a three-dimensional solid model was established by using the finite difference software FLAC3D to simulate the stress states and displacement states of the surrounding rock under different fracturing heights and directions. The stress and displacement were compared and analyzed to determine the optimal slitting parameters.

6.1 Establishing the FLAC3D Three-Dimensional Numerical Model

The numerical simulation model is shown in Fig. 8. The model size was $178 \text{ m} \times 200 \text{ m} \times 32 \text{ m}$ (length, width, height), and this was divided into 600,556 grid cells and 666,528 nodes. The slits in the numerical simulation were used to simulate the roof cutting by refining the cells and by grouping and excavating the cells where the tangential line was located. The lateral displacement of the model was limited, the bottom was fixed, the upper surface was the stress boundary, and the vertical load was 7.9 MPa, simulating the self-weight boundary of the overlying strata (Sitharam et al. 2007). The material damage met the Mohr–Coulomb strength criteria.

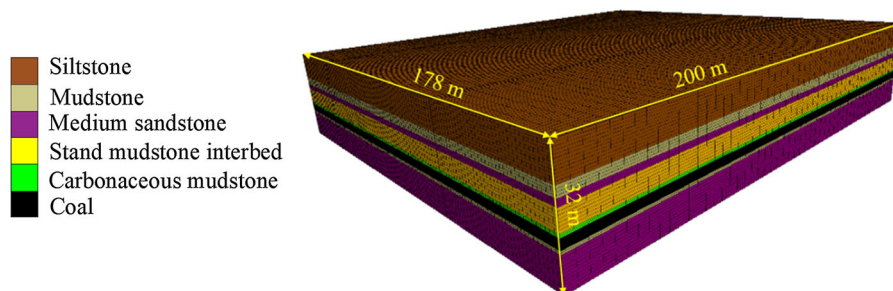


Fig. 8 Numerical simulation model

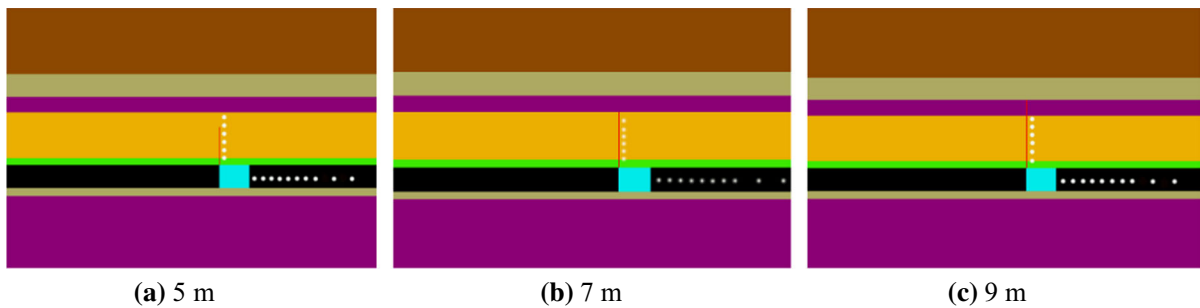


Fig. 9 The calculation models

6.2 The Result of the Numerical Simulation

The roof fracturing heights investigated were 5 m, 7 m, and 9 m, and the roof fracturing direction was 0° . In order to reflect the change in the stress and displacement of the surrounding rock more intuitively, six and ten monitoring points were arranged in the roof near the gob side and in the right pillar of the roadway, respectively, to monitor the displacement and stress changes of the surrounding rock. The calculation models for different roof fracturing heights are shown in Fig. 9, and the calculated results of the stress and displacement nephograms are shown in Figs. 10 and 11.

From Fig. 10a, it can be seen that the stress concentration area of the surrounding rock decreases and moves deeper into the surrounding rock with increased roof fracturing height, which improves the stress of the rock surrounding the roadway. This shows that directional pre-splitting blasting cuts off the stress transfer path between the roadway and the roof of the gob and reduces the influence of the basic roof rotation deformation. However, with increased cutting height, the extrusion stress of the roadway's immediate roof increases slightly.

According to the stress monitoring data, as shown in Fig. 10b, the stress value of the surrounding rock in the right-hand side of the roadway decreases with increasing roof fracturing height, and the peak stress value decreases by nearly 2–3 MPa. For example, when the cutting height is 5 m, the peak stress is 20.3 MPa, while it is 18.2 MPa with a 7 m roof fracturing height and 16.9 MPa with a 9 m roof fracturing height.

From Fig. 11, it can be seen that the roof subsidence of the roadway decreases with increasing roof fracturing height, and the reduction value is nearly

80–120 mm. For example, the roof subsidence is 300 mm when the roof fracturing height is 5 m, while it is 220 mm with a 7 m roof fracturing height and 178 mm with a 9 m roof fracturing height.

From the above calculation results, it can be seen that the stress value of the surrounding rock and the roof subsidence are the largest with a 5 m roof fracturing height; they are not very different when the roof fracturing height is 7 m or 9 m. Considering the difficulties involved with construction technology and the economic benefits, the cutting height was finally determined to be 7 m.

The roof fracturing height used in the simulation calculation was 7 m, and the roof fracturing directions were 0° , 15° , and 20° . We determined the best cutting angle by analyzing the stress variation in the surrounding rock under different cutting angles. The calculation models of the different roof fracturing directions are shown in Fig. 12.

The results of the different roof fracturing direction calculations are shown in Figs. 13 and 14. By comparing and analyzing the stress distributions and the displacement distributions for different fracturing directions, the following results were obtained:

1. It can be seen from Fig. 13a that the directional pre-splitting blasting cuts the stress transfer between the roadway and the gob. The surrounding rock stress of the roadway was improved, and the concentrated stress area of the surrounding rock was transferred to the depth of the surrounding rock.
2. By comparing the stress nephograms of different fracturing directions, it was found that as the roof fracturing angle increases, the stress concentration area of the surrounding rock is transferred deeper and the peak stress decreases. Different ranges of

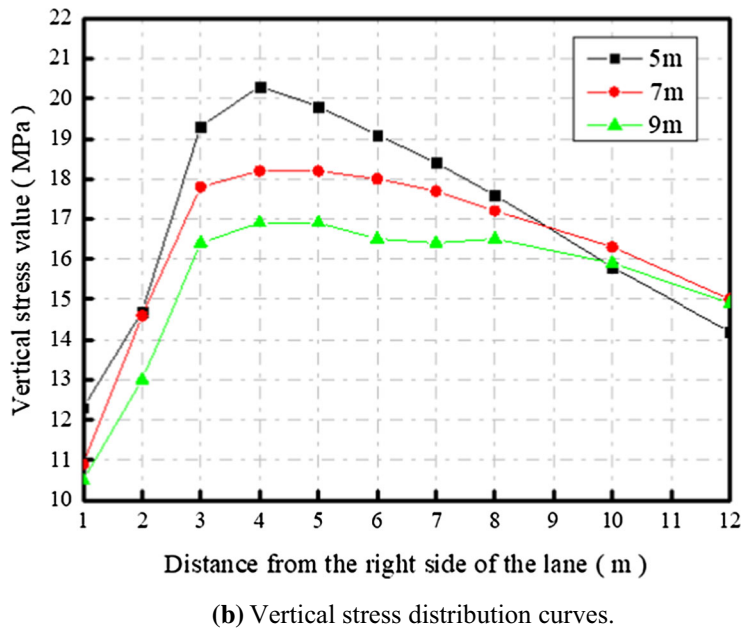
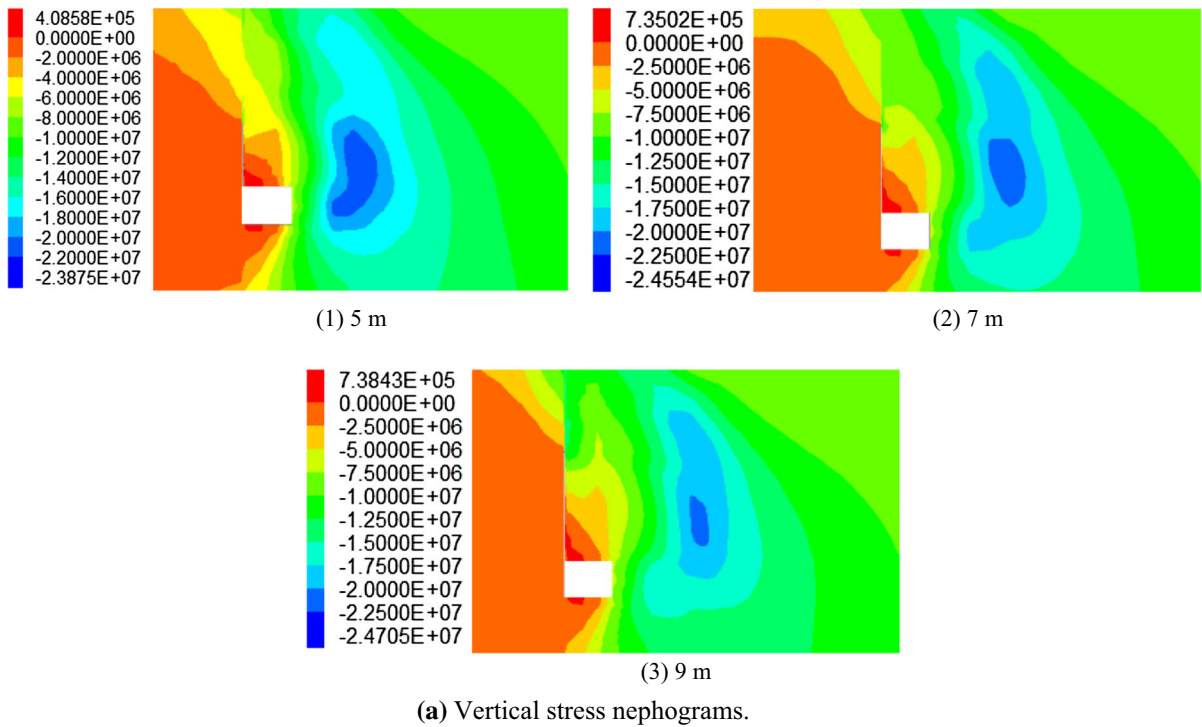
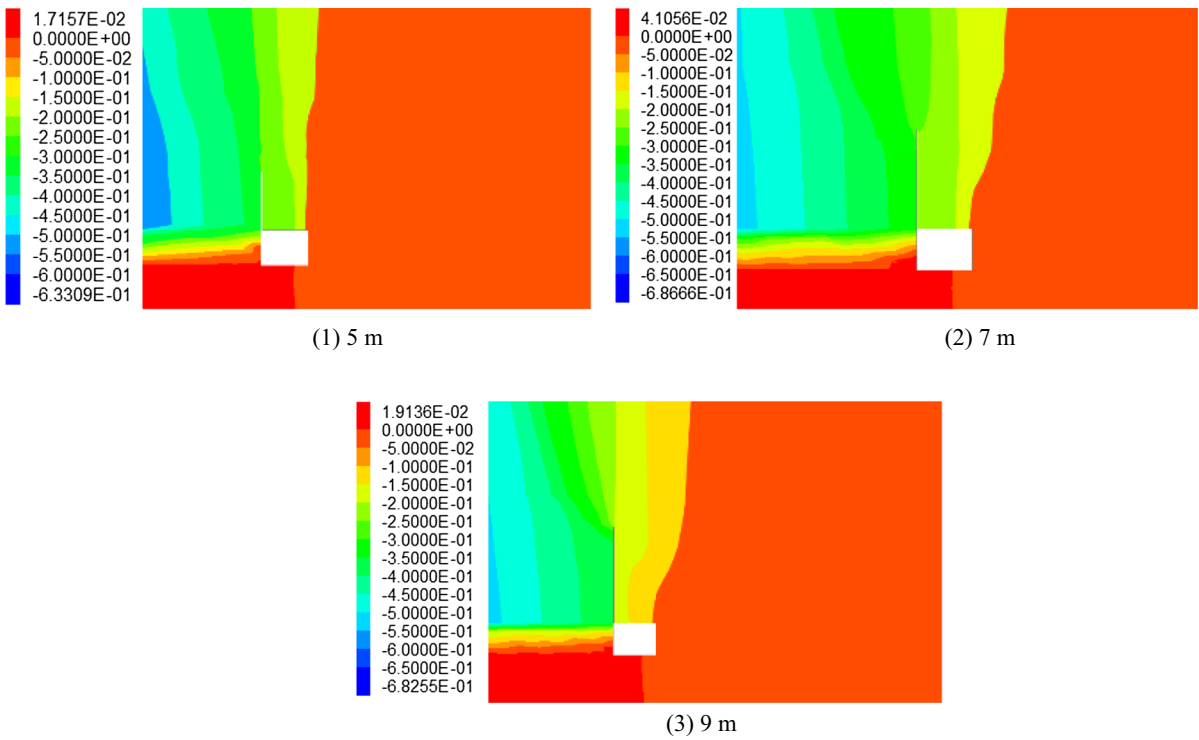


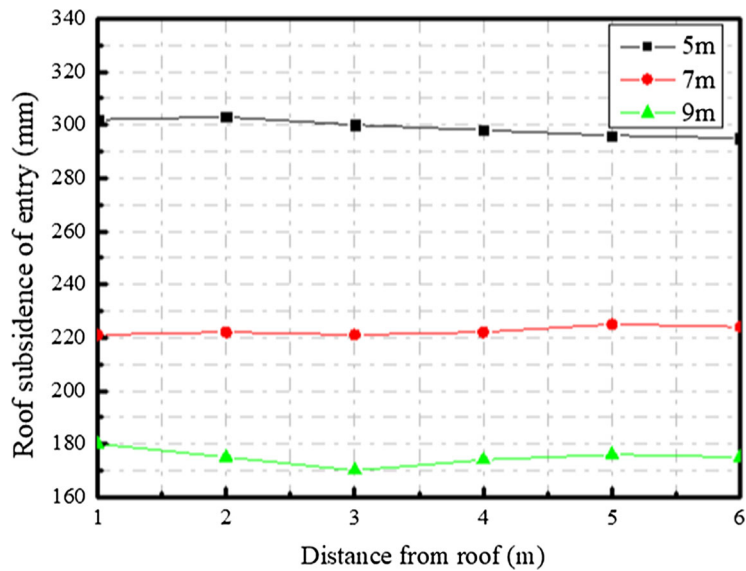
Fig. 10 Vertical stress nephograms and vertical stress distribution curves

compressive stress concentration appeared on both sides of the 0°, 15°, and 20° fracture surfaces, indicating that when the roof of the roadway sinks after cutting, extrusion stress is produced by

extrusion between the roadway roof and the gangue of the gob. It can be seen from the stress nephogram that the compressive stress on both sides of the 20° fracture surface is the largest,



(a) Vertical displacement distributions.



(b) Vertical displacement distribution curves.

Fig. 11 Vertical displacement nephograms and vertical displacement curves

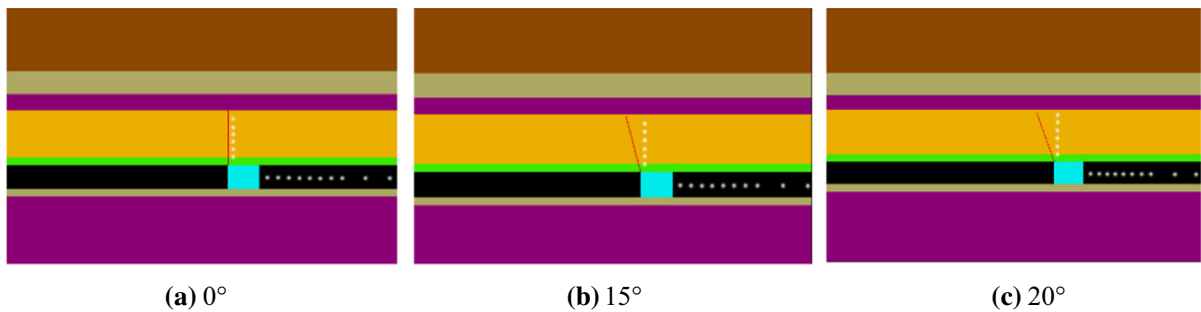


Fig. 12 The calculation models

- indicating that the larger the cutting angle, the greater the compressive stress on the immediate roof.
3. From Fig. 13b, we can see that a certain fracturing direction can improve the stress state of the surrounding rock and reduce the stress by nearly 1 MPa. However, when compared with the roof fracturing angles of 15° and 20°, the change in the surrounding rock stress is not obvious.
 4. It can be concluded from Fig. 14 that the roof subsidence of the roadway decreases slightly with an increase in the roof fracturing angle. For instance, the roof subsidence is nearly 225 mm when the roof fracturing angle is 0°, nearly 208 mm with a 15° roof fracturing angle, and nearly 206 mm with a 9 m roof fracturing angle.
 1. In summary, for the 12,605 working face of Guandi Coal Mine, the best fracturing direction is 15°.

7 Engineering Applications

According to the theoretical analysis and numerical simulation, the optimum fracturing height and fracturing direction are 7 m and 15°, respectively. This test adopted the directional pre-splitting blasting method with a drilling distance of 500 mm, and the specially shaped energy tube had an outer diameter of 42 mm, an inner diameter of 36.5 mm, and a tube length of 1500 mm. Three-stage Emulsified Explosive is Used in Coal Mines for energy-accumulating blasting. The following explosive specifications are proposed: diameter $\Phi 32 \times 200$ mm/volume, four energy-accumulating tubes installed in each blasting borehole, three of them 1.5 m in length, a 0.5 m long

condenser tube, and 2 m long mud sealing at the orifice. The specific charge quantity and blasting mode were determined according to the field test results as 3, 3, 2, and 1 charge coils in the four energy-accumulating tubes per hole and observation mode circulation of five charge holes and one hole for five charge holes. For one Detonation of a 10-hole Joint Gun, the charge structure is shown in Fig. 15.

In order to ensure the stability of the roadway during the process of roof cutting and the period of pressure, the roadway roof was reinforced using a CRLDA before pre-splitting and cutting. To make the constant resistance anchor cable play a better suspension role in the process of retaining the roadway and to effectively protect the anchor end, the length of a constant resistance anchor cable is generally designed to be H joint + 2.3 m, and we ensure that the anchor end is located in a relatively stable rock layer. The CRLDA were vertically arranged in the direction of the roof, and there were three columns in total. The first row of CRLDA was 500 mm away from the roadway, and the row spacing was 1000 mm; the second row was 1500 mm from the front, and the row spacing was 6000 mm; the third row was arranged 1200 mm away from the auxiliary side, and the row spacing was 6000 mm. The roadway support is shown in Fig. 16. The roof of the gob will have a certain frictional effect on the roof of the roadway, the roadway will be affected by the dynamic pressure, and the pressure on the roof will be greater. Therefore, the roof needs temporary reinforcement. Four single pillars were arranged in each row, with a row spacing of 500 mm, and were mainly arranged on the side of the roadway. Four single hydraulic props were arranged in each row, with a row spacing of 500 mm, and were mainly arranged on the side of the roadway. In order to control the fallen gangue, it is

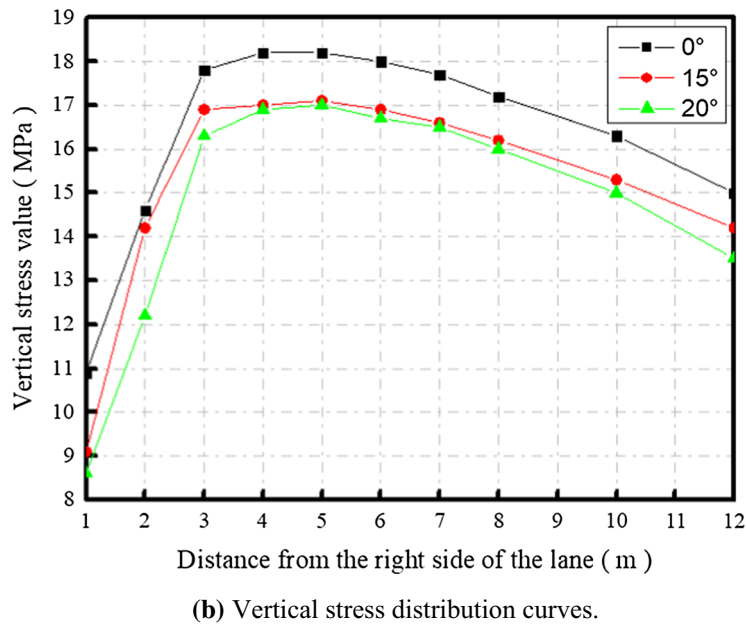
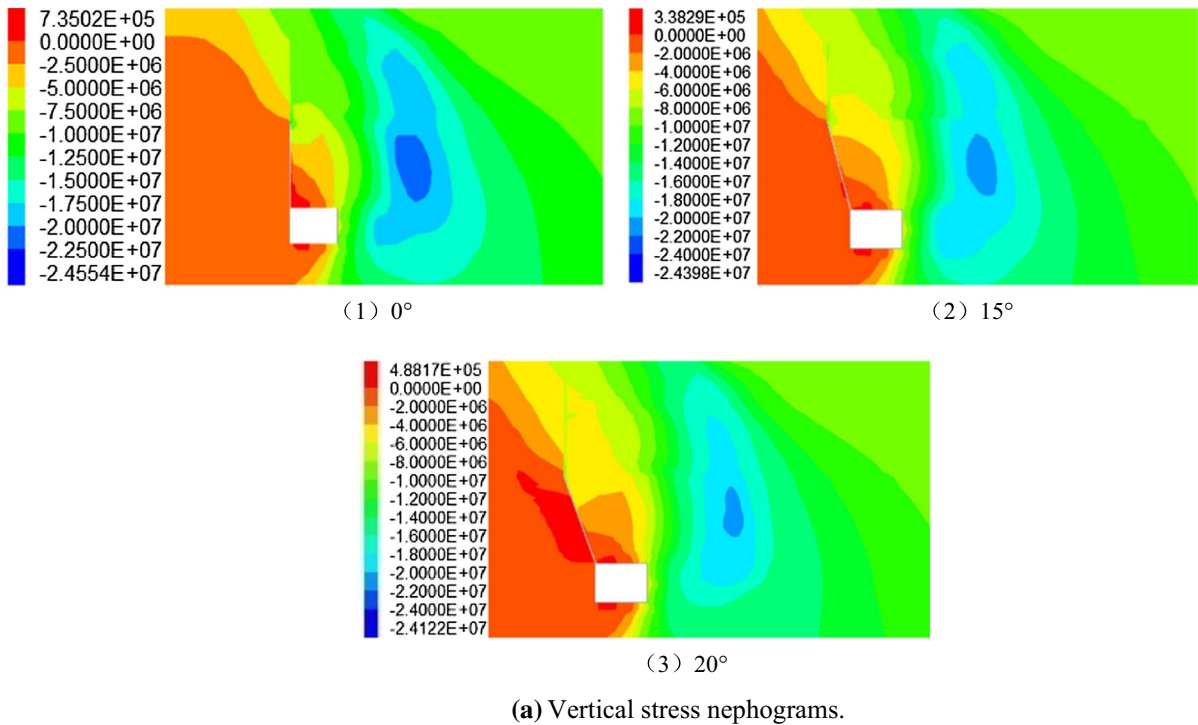
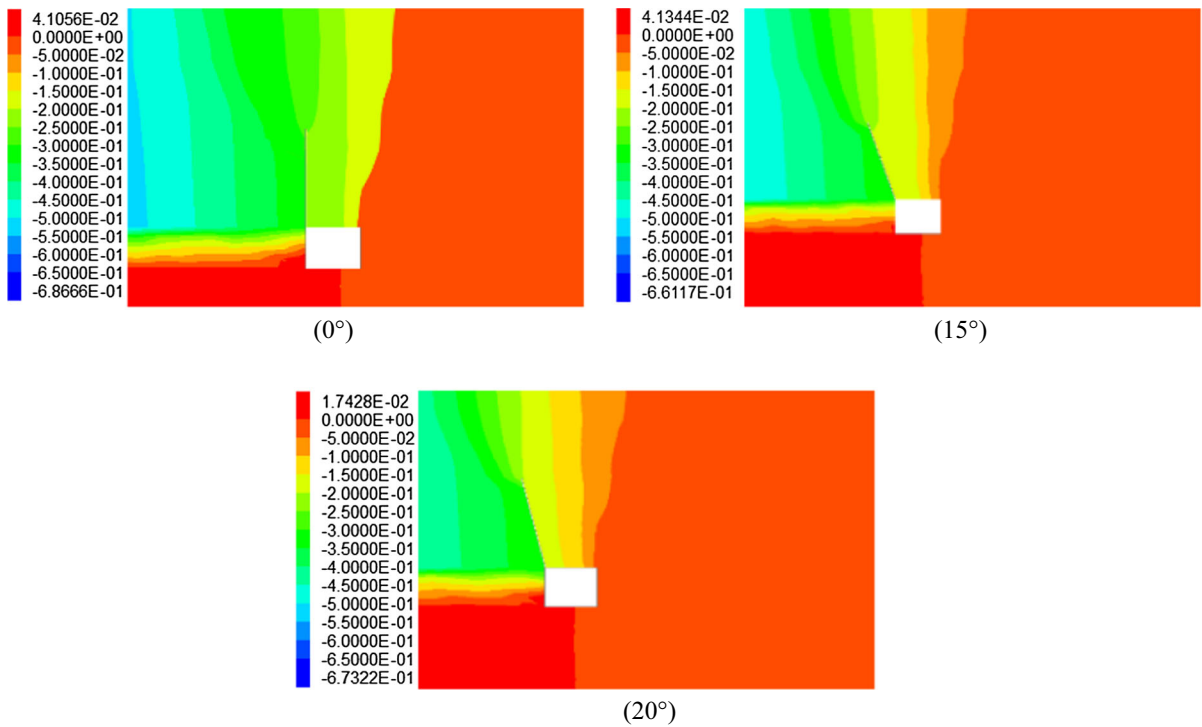


Fig. 13 Vertical stress nephograms and vertical stress distribution curves

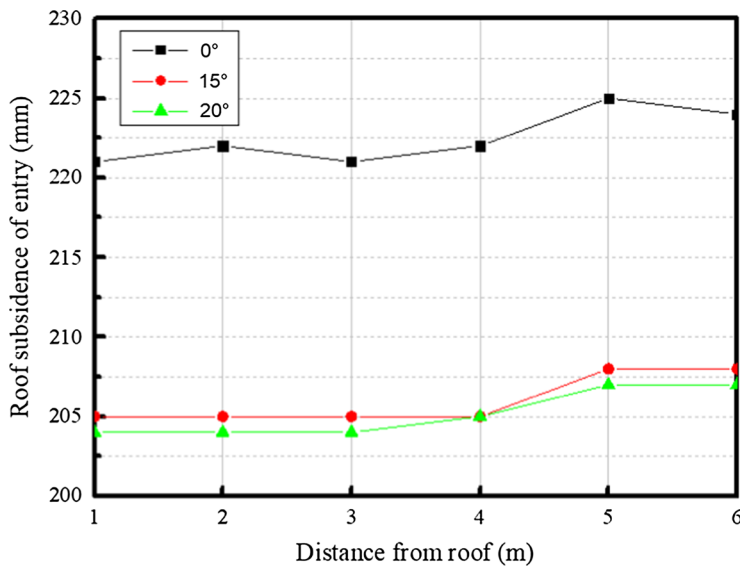
necessary to install a gangue wall maintaining support. The gangue retaining support was implemented by means of steel mesh, a single hydraulic prop, and

telescopic U-shaped steel. The cross-sectional layout of the supporting structure is shown in Fig. 16.

The rock deformation surrounding the roadway can well reflect whether the rock surrounding the roadway



(a) Vertical displacement distributions.



(b) Vertical displacement distribution curves.

Fig. 14 Vertical displacement nephograms and vertical displacement curves

has reached a stable state. Therefore, during the roadway retention at the 12,605 working face, the crisscross method for monitoring the surrounding rock

was adopted; the locations of the displacement monitoring points are shown in Fig. 16 and the monitoring data are shown in Fig. 17.

Fig. 15 Charge structure

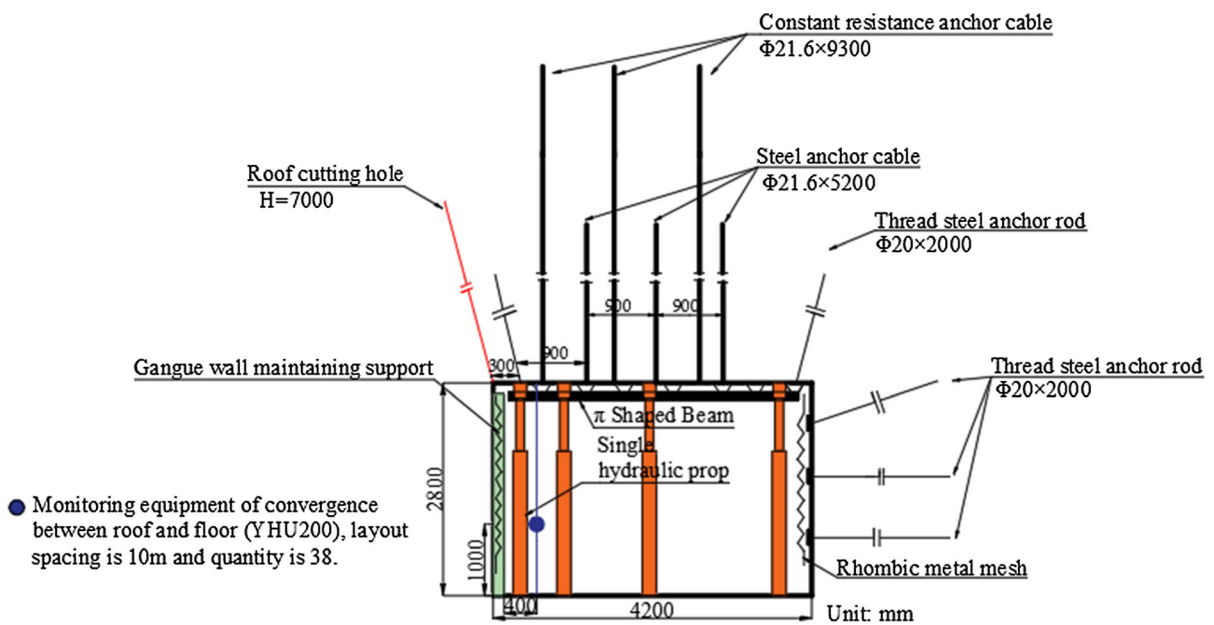
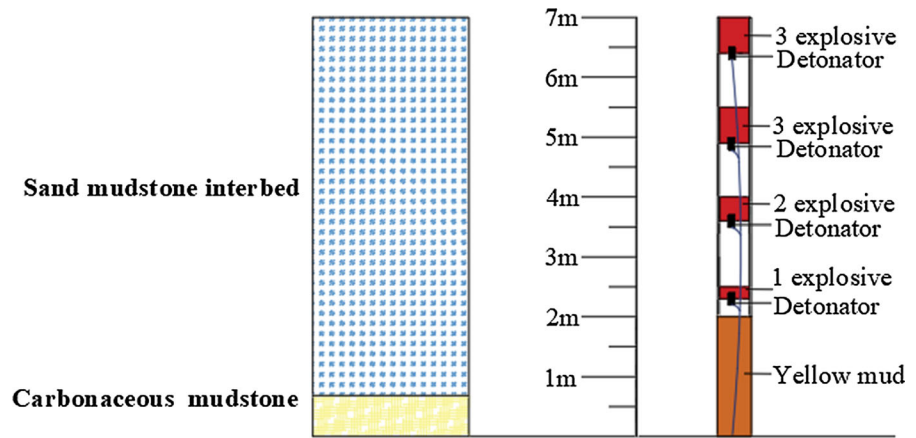


Fig. 16 The cross-sectional layout of the supporting structure

It can be seen from Fig. 17 that the roof and floor of the roadway began to deform at 30 m ahead of the working face and were severely deformed within 30–100 m behind the working face; finally, they reached a steady state at 200 m behind the work surface. The field test monitoring data show that the

deformation of the roadway was mainly caused by the subsidence of the roof. The final subsidence of the roof was 205 mm, and the floor heave was 65 mm. The results verify the validity of the numerical simulation results, as shown in Fig. 18.

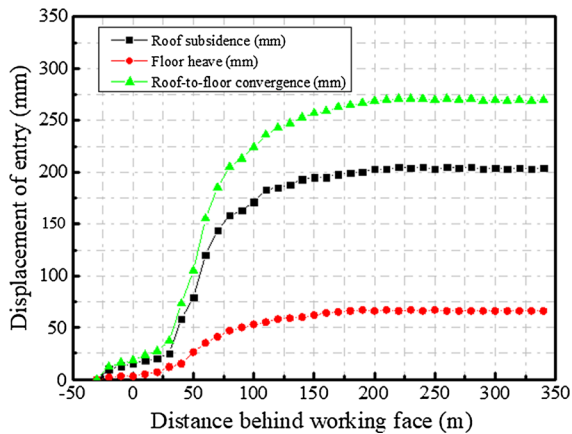


Fig. 17 Deformation of the surrounding rock

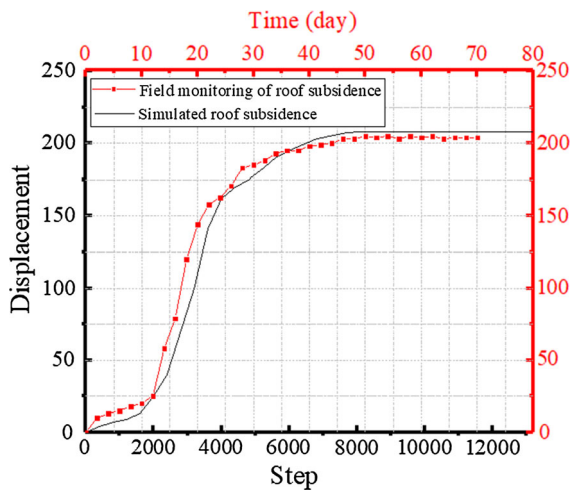


Fig. 18 Comparison between the measured and simulated displacement

8 Conclusions

1. In order to study the factors leading to roof subsidence, the relationships between different

factors and roof subsidence were analyzed by establishing a mechanical model. It is concluded that the main factors affecting roof subsidence are the rotation angle of the upper main roof, the fracturing height, and the roof fracturing direction. Increasing the support strength in the roadway has less influence on roof deformation. Therefore, roof subsidence can be effectively controlled by controlling the rotation of the basic roof and by increasing the height and angle of the cutting roof.

2. The numerical simulation results show that the stress transfer path between the roof of the roadway and the roof of the gob is cut by the directional pre-splitting blasting; further, the stress state of the surrounding rock is improved, and the concentrated stress area of the surrounding rock is transferred to a deeper part. Compared with a vertical slit, under a certain fracturing direction, the concentrated stress area of the surrounding rock is farther away from the roadway, the concentrated stress value is significantly reduced, and the stress state of the surrounding rock is further improved. A certain fracturing direction reduces the friction of the roof, which is better for the roof of the gob. Due to the disturbance of the fallen gangue in the gob, the roof of the roadway near the gob sunk obviously.
3. An analysis of the displacement deformation monitoring data showed that due to the influence of the pre-pressure, the roof and floor of the roadway started to deform at 30 m in front of the working face. The deformation of the roof in the range of 30–110 m behind the working face was caused by the strong disturbance of the gangue. When the gangue in the gob was compacted and stabilized, the rock surrounding the roadway was basically in a stable state.

Acknowledgements This work was supported by the National Natural Science Foundation of China (No. 41672347). We also express our thanks to the reviewers for their time and effort on reviewing this paper.

Compliance with Ethical Standards

Conflicts of interest The authors declare that they have no conflict of interest.

References

- Chen JH, Zhang JS, Li XP (2016) Study of presplitting blasting parameters and its application based on rock blasting-induced damage theory. *Rock Soil Mech* 37(5):1441–1450 (in Chinese)
- Deng YH, Wang SQ (2014) Feasibility analysis of gob-side entry retaining on a working face in a steep coal seam. *Int J Min Sci Technol* 24(4):499–503
- Gao F, Qian MG, Miao XX (2000) Mechanical analysis of the immediate roof subjected to given deformation of the main roof. *Chin J Rock Mech Eng* 19(2):145–148 (in Chinese)
- Gao YB, Guo ZB, Yang J, Wang JW, Wang YJ (2017) Steady analysis of gob-side entry retaining formed by roof fracturing and control techniques by optimizing mine pressure. *J China Coal Soc* 42(7):1672–1681 (in Chinese)
- Gao YB, He MC, Yang J, Ma XG (2018) Experimental study of caving and distribution of gangues influenced by roof fracturing in pillarless mining with gob-side entry retaining. *J China Univ Min Technol* 47(1):21–31 and 47 (in Chinese)
- Guo PF, Zhang GF, Tao ZG (2016) Blasting technology of gateway retaining along gob pressure release by roof cutting in hard and weak complex roof. *Coal Sci Technol* 44(10):120–124 (in Chinese)
- Han CL, Zhang N, Ran Z, Gao R, Yang HQ (2018a) Superposed disturbance mechanism of sequential overlying strata collapse for gob-side entry retaining and corresponding control strategies. *J Cent South Univ* 25(9):2258–2271
- Han CL, Zhang N, Xue JH, Kan JG, Zhao YM (2018b) Multiple and long-term disturbance of gob-side entry retaining by grouped roof collapse and an innovative adaptive technology. *Rock Mech Rock Eng*. <https://doi.org/10.1007/s00603-018-1612-0>
- He MC, Zhu GL, Guo ZB (2015) Longwall mining “cutting cantilever beam theory” and 110 mining method in China—the third mining science innovation. *J Rock Mech Geotech Eng* 7(5):483–492
- He MC, Gao YB, Yang J, Gong WL (2017a) An innovative approach for gob-side entry retaining in thick coal seam longwall mining. *Energies* 10(11):1785
- He MC, Chen SY, Guo ZB, Yang J, Gao YB (2017b) Control of surrounding rock structure for gob-side entry retaining by cutting roof to release pressure and its engineering application. *J China Univ Min Technol* 46(5):959–969 (in Chinese)
- He MC, Wang YJ, Yang J, Zhou P, Gao Q, Gao YB (2018a) Comparative analysis on stress field distributions in roof cutting non-pillar mining method and conventional mining method. *J China Coal Soc* 43(3):626–637 (in Chinese)
- He MC, Ma ZM, Guo ZB, Chen SY (2018b) Key parameters of the gob-side entry retaining formed by roof cutting and pressure release in deep medium-thickness coal seams. *J China Univ Min Technol* 47(3):468–477 (in Chinese)
- Lin HL, Shi YK (2012) Research on walling-up with concrete block technology of gob-side entry retaining based on fully mechanized face in medium-thickness coal seam. *Appl Mech Mater* 121–126:2878–2882
- Lu XY, Hua XZ, Zhao MQ (2011) Calculation and analysis of immediate roof subsidence in gob-side entry retaining. *J Min Saf Eng* 28(1):34–38 (in Chinese)
- Ma XG, He MC, Wang J, Zhu XQ, Li CL, Zhang JB, Jiang QQ (2017) Study on design of chamber supporting behind cutting hole under condition of gob-side entry retaining in 8304 face of Yanya coal mine. *Coal Technol* 36(12):30–33 (in Chinese)
- Ma XG, He MC, Sun JD, Hu J, Zhang XY, Zhang JB (2018a) Research on the design of roof cutting parameters of non-coal pillar gob-side entry retaining mining with roof cutting and pressure releasing. *Geotech Geol Eng* 37:1169–1184
- Ma XG, He MC, Sun JD, Wang HH, Liu XY, Zhen EZ (2018b) Neural network of roof cutting blasting parameters based on mines with different roof conditions. *Energies* 11(12):3468
- Qian MG, Miao XX (1996) New development of face underground pressure theory. *Ground Press Strata Control* 13(2):17–20 (in Chinese)
- Qian MG, Miao XX, He FL, Liu CY (1996) Mechanism of coupling effect between supports in the workings and the rocks. *J China Coal Soc* 21(1):40–44 (in Chinese)
- Sitharam TG, Maji VB, Verma AK (2007) Practical equivalent continuum model for simulation of jointed rock mass using FLAC3D. *Int J Geomech* 7(5):389
- Sun XM, Liu X, Liang GF, Wang D, Jiang YL (2014) Key parameters of gob-side entry retaining formed by roof cut and pressure releasing in thin coal seams. *Chin J Rock Mech Eng* 33(7):1449–1456 (in Chinese)
- Waclawik P, Kukutsch R, Konicek P, Ptacek J et al (2017) Stress state monitoring in the surroundings of the roadway ahead of longwall mining. *Procedia Eng* 191:560–567
- Wang XY, Shang DY, Liu N, Li SY, Fan X (2014) Analysis design and roof motion track simulation for gob-side entry retaining hydraulic support. *Appl Mech Mater* 633–634:1244–1247
- Wang YJ, Gao YB, Wang EY, He MC, Yang J (2018) Roof deformation characteristics and preventive techniques using a novel non-pillar mining method of gob-side entry retaining by roof cutting. *Energies* 11(3):627
- Xu Y, Chen J, Bai JB (2016) Control of floor heaves with steel pile in gob-side entry retaining. *Int J Min Sci Technol* 26(3):527–534
- Yang HY, Cao SG, Wang SQ, Fan YC, Wang S, Chen XZ (2016) Adaptation assessment of gob-side entry retaining based on geological factors. *Eng Geol* 209:143–151
- Zhang N, Yuan L, Han CL, Xue JH, Kan JG (2012) Stability and deformation of surrounding rock in pillarless gob-side entry retaining. *Saf Sci* 50(4):593–599
- Zhang ZZ, Bai JB, Chen Y, Yan S (2015) An innovative approach for gob-side entry retaining in highly gassy fully-

mechanized longwall top-coal caving. *Int J Rock Mech Min Sci* 80:1–11

Zhang ZZ, Wang WJ, Li SQ, Yu XY (2018) Analysis on rockbolt support interaction with roof dilatancy above roadside backfill area in gob-side entry retaining. *Geotech Geol Eng* 36(4):2577–2591

Publisher's Note Springer Nature remains neutral with regard to jurisdictional claims in published maps and institutional affiliations.